

Rank-Aware Spectral Bounds on Attention Logits for Stable Low-Precision Training

Seyed Morteza Emadi¹

Abstract

Attention scores in transformers are bilinear forms $S_{ij} = x_i^\top M x_j / \sqrt{d_h}$ whose maximum magnitude governs overflow risk in low-precision training. We derive a *rank-aware concentration inequality*: when the interaction matrix $M = W^Q W^{K\top}$ has rank $r \ll d$, tail probabilities for $\max_{i,j} |S_{ij}|$ decay as $\exp(-d^2 \alpha^2 / (\gamma r))$ rather than $\exp(-d \alpha^2)$, where $\gamma > 1$ is a typicality parameter. For transformer attention where $r = d_h$, this yields 8–28× tighter concentration than rank-agnostic bounds in modern architectures. We apply this result to FP8 training, deriving *geometry-aware scale factors* that provide principled overflow guarantees without observing activations. The method computes per-layer scales from the spectral norm $\|W^Q W^{K\top}\|_2$ via implicit power iteration, includes a grouped query attention formulation that avoids key expansion, and remains compatible with fused attention kernels. Across GPT-2 XL to Llama-2-70B, geometry-aware scaling eliminates overflows in transient scenarios where delayed scaling fails, while achieving comparable downstream MMLU accuracy.

1. Introduction

Attention logits in transformers exhibit a bilinear structure: each score $S_{ij} = x_i^\top W^Q W^{K\top} x_j / \sqrt{d_h}$ depends on the interaction of two projected vectors. This structure determines the maximum magnitude of attention logits, a quantity with direct consequences for low-precision training. FP8 formats reduce precision from 16 to 8 bits, but the E4M3 format spans only ± 448 compared to FP16’s $\pm 65,504$.¹ When attention logits exceed this range, quantization overflows

¹UNC-Chapel Hill, Kenan-Flagler Business School, Chapel Hill, NC, USA. Correspondence to: Seyed Morteza Emadi <seyed.emadi@kenan-flagler.unc.edu>.

¹FP8 training can yield substantial speedups on memory-bound workloads (Micikevicius et al., 2022); our focus is on the calibration problem that enables safe deployment.

produce NaN values that corrupt training.

Problem formulation. Let R_{\max} denote the representable range of the target format ($R_{\max} = 448$ for E4M3). Given a scale factor $s > 0$, quantization overflows when $\max_{i,j} |S_{ij}| > s \cdot R_{\max}$. The calibration problem is to select s that:

1. **(Safety)** Ensures $\Pr(\max_{i,j} |S_{ij}| > s \cdot R_{\max}) \leq \delta^*$ for a target failure probability δ^* ;
2. **(Utilization)** Maximizes precision utilization $\mathbb{E}[\max_{i,j} |S_{ij}|] / (s \cdot R_{\max})$, minimizing quantization error.

These objectives trade off: smaller s improves utilization but increases overflow risk. The challenge is to calibrate s *without observing* $\max_{i,j} |S_{ij}|$, which would require materializing the full attention matrix.

Existing methods derive scale factors from *observed* activation statistics, either from a history buffer (delayed scaling) or per-iteration (current scaling), without analyzing the bilinear mechanism that governs logit magnitudes.

Delayed scaling and its limitations. The standard approach for FP8 training is *delayed scaling* (Micikevicius et al., 2022), which maintains a history buffer of activation maxima (typically 16 steps) and derives scale factors from past observations:

$$\text{scale}_t = \frac{\max(\text{history})}{448 \cdot \eta}, \quad (1)$$

where $\eta < 1$ provides a safety margin. Scale factors are computed *before* the current forward pass, avoiding the need to observe current activations.

However, delayed scaling assumes activation magnitudes change slowly. This assumption breaks whenever weight dynamics outpace the history buffer. We call this failure mode *history staleness*. Common triggers include: (i) loading pretrained checkpoints, where FP8 history initializes to defaults while weights reflect extensive prior training; (ii) resuming from saved states, since standard checkpointing omits scaling state; and (iii) learning rate transitions, where

warmup or cyclic schedules cause weights to shift faster than history adapts. An alternative is *current scaling*, which computes scale factors from $\max |S_t|$ in each forward pass. This eliminates staleness but requires materializing the full $L \times L$ attention score matrix, incompatible with fused attention kernels like FlashAttention (Dao et al., 2022; Dao, 2024) that achieve $O(L)$ memory precisely by avoiding this materialization.

Table 1 summarizes this dilemma: delayed scaling is compatible with fused kernels but fails during transients; current scaling handles transients but requires materializing the score matrix. Prior to this work, no method achieved both.

Table 1. The FP8 scaling dilemma.

Method	Transient-Safe	Fused-Compat.
Delayed	✗	✓
Current	✓	✗
Ours	✓	✓

Our approach: predictive calibration from weight geometry. We propose a fundamentally different paradigm. Instead of *reacting* to observed activations (whether past or present), we *predict* their bounds from the singular value structure of the query-key interaction matrix. Attention scores form a bilinear structure:

$$S_{ij} = \frac{x_i^\top M x_j}{\sqrt{d_h}}, \quad \text{where } M = W^Q W^{K^\top} \in \mathbb{R}^{d \times d} \quad (2)$$

is the query-key *interaction matrix* and x_i, x_j are input embeddings. For *pre-LN architectures* (including GPT-2, Llama, and Mistral, which place normalization before attention), LayerNorm (or RMSNorm (Zhang & Sennrich, 2019)) constrains $\|x_i\| \approx \sqrt{d}$, yielding:

$$\max_{i,j} |S_{ij}| \leq \|M\|_2 \cdot \frac{d}{\sqrt{d_h}} =: B_{\max}. \quad (3)$$

This bound depends only on current weights, not activations, and can be estimated via power iteration (Golub & Van Loan, 2013) without forming the $d \times d$ matrix M . When weights change, the bound updates immediately, enabling *predictive* calibration that eliminates the failure modes of delayed scaling during transients such as checkpoint loading, resumption, and learning rate changes. Since we never observe activations, compatibility with fused attention kernels is preserved.

The worst-case bound B_{\max} assumes inputs align perfectly with top singular vectors, which becomes exponentially unlikely as dimension increases. We therefore introduce a calibration factor $\alpha \in (0, 1)$ to obtain a tighter bound $B_\alpha = \alpha \cdot B_{\max}$. To quantify the associated risk, we derive a *rank-aware concentration inequality* on $\Pr(\max_{i,j} |S_{ij}| \geq B_\alpha)$ that exploits the low-rank structure of the interaction

matrix ($\text{rank}(M) = d_h \ll d$). The key insight is that although M acts on d -dimensional space, its range is only d_h -dimensional; inputs are exponentially unlikely to find this low-dimensional subspace of maximum amplification. The resulting tail exponent improves from $d\alpha^2$ to $d^2\alpha^2/(\gamma d_h)$, a factor of $d/(\gamma d_h) = 8\text{--}28\times$ in modern architectures (where $\gamma > 1$ is a parameter controlling the typicality threshold; see Section 3.2). This analysis provides a principled selection rule: given a target overflow probability δ^* , we derive the minimum α guaranteeing $\Pr(\max_{i,j} |S_{ij}| \geq B_\alpha) \leq \delta^*$.

Contributions.

- Tight spectral interaction bound.** We prove $\max_{i,j} |S_{ij}| \leq \|W^Q W^{K^\top}\|_2 \cdot d/\sqrt{d_h}$ under the distributional constraints induced by LayerNorm or RMSNorm. This bound is never looser than the naive submultiplicative bound $\|W^Q\|_2 \|W^K\|_2$ and is strictly tighter unless the top right singular vectors align (Corollary 3.3). We show extension to RoPE architectures, with the tighter interaction bound validated empirically (Corollary 3.6).
- Rank-aware concentration inequality.** We prove a concentration inequality for bilinear forms $x_i^\top M x_j$ when M has rank $r \ll d$ and inputs are approximately uniform on the sphere (Proposition 3.4). The key insight is a two-stage conditioning argument: first bound the probability that projections onto M 's row space are atypical, then apply concentration with a tighter Lipschitz constant. This yields tail exponents of order $d^2\alpha^2/(\gamma r)$ versus $d\alpha^2$ for rank-agnostic bounds, an improvement of $d/(\gamma r)$ that becomes $8\text{--}28\times$ in modern transformers where $r = d_h$. Applied to attention, this provides a principled selection rule: given a target overflow probability δ^* , we derive the minimum calibration factor α guaranteeing safety.
- Implicit spectral norm estimator.** We estimate $\|W^Q W^{K^\top}\|_2$ via power iteration without forming the $d \times d$ interaction matrix, achieving $O(n_{\text{heads}} \cdot d_h \cdot d)$ cost per layer. For grouped query attention, we derive an implicit formulation that avoids key matrix expansion (Section 4.2).
- Empirical validation.** Zero overflows across GPT-2 XL through Llama-2-70B on all transient scenarios where delayed scaling fails. Downstream evaluation on MMLU confirms preserved capability: our auto- α calibration achieves accuracy comparable to delayed scaling (33.6% vs. 33.0%) while eliminating all overflows, whereas conservative spectral bounds degrade to 28.1% due to under-utilization (Section 5.4).

Positioning. The spectral bound in Equation (3) builds on classical matrix analysis; our contribution lies in developing

a complete calibration framework for low-precision training. This requires solving three problems that the bound alone does not address: (i) principled probabilistic calibration under the rank-deficient structure of attention, (ii) efficient per-layer computation via implicit power iteration, and (iii) an implicit GQA formulation that avoids key expansion. Together, these enable the first calibration method that is both robust to transients and compatible with fused attention kernels.

2. Related Work

FP8 training and scaling strategies. Micikevicius et al. (2022) introduced FP8 formats and delayed (history-based) scaling, now standard in low-precision training frameworks. DeepSeek-V3 (DeepSeek-AI, 2024) employs per-tile scaling (e.g., 1×128 blocks) but retains attention in BF16/FP32. Microscaling (Rouhani et al., 2023) similarly uses block-wise factors. These approaches address *spatial heterogeneity* within tensors but still derive scales from observed values, inheriting history staleness during transients. FlashAttention-3 (Shah et al., 2024) introduces native FP8 support with internal block quantization, but requires inputs cast to FP8 *before* kernel entry. Incorrect global scale factors cause overflow before internal mechanisms can compensate. Other recent work addresses orthogonal aspects: architectural modifications (Hernández-Cano et al., 2025), inference fallback (Lee et al., 2025), and LoRA fine-tuning (Choi et al., 2025). Our method provides a *safety envelope*: geometry-aware bounds ensure inputs are within safe range, and are orthogonal to block-wise optimizations.

Predictive scaling. Unit Scaling (Blake et al., 2023) eliminates scaling factors via careful initialization that maintains unit variance throughout the network, but requires training from scratch and cannot be applied to pretrained checkpoints. MOSS (Zhang et al., 2025) exploits the bounded update property of AdamW ($|\Delta W_t| \leq \eta$) to predict *weight* magnitudes without runtime max-reduction. However, MOSS requires the MXFP8 microscaling format with hardware-specific support. More fundamentally, bounds derived from individual weight norms $\|W^Q\|$ and $\|W^K\|$ are too loose for effective FP8 calibration: the naive bound $\|W^Q\|_2 \|W^K\|_2$ can substantially overestimate when singular vectors of W^Q and W^K do not align, wasting dynamic range (Corollary 3.3). Our method addresses attention-specific overflow using only the standard E4M3 format, requires no custom kernels, and is compatible with NVIDIA’s Transformer Engine.

Spectral methods for transformer stability. Zhai et al. (2023) show that *entropy collapse* (attention concentrating on single tokens) is governed by the spectral norm of the query-key interaction matrix. Our work reveals the same quantity governs numerical overflow risk, connecting optimization stability and numerical stability through shared

geometric structure. Miyato et al. (2018) introduced spectral normalization for GANs as a regularizer; we use spectral norms for *prediction* rather than constraint.

3. Theoretical Foundation

This section develops the theoretical basis for geometry-aware scaling.

3.1. Spectral Bound on Attention Logits

Pre-softmax attention scores are computed as $S = QK^\top / \sqrt{d_h}$, where $Q = XW^Q$ and $K = XW^K$. Each score can be written as:

$$S_{ij} = \frac{x_i^\top M x_j}{\sqrt{d_h}}, \quad \text{where } M = W^Q W^{K^\top} \in \mathbb{R}^{d \times d}. \quad (4)$$

The matrix M is the *query-key interaction matrix*. Unlike FFN layers (additive structure) or embeddings (element-wise), attention’s *bilinear* structure compounds magnitudes: large queries meeting large keys produce scores that can exceed the E4M3 threshold of 448. This makes attention the primary overflow bottleneck in FP8 training.

To bound attention logits, we exploit this bilinear structure. Proofs for this section are in Appendix A. A natural first approach tracks $\|W^Q\|_2$ and $\|W^K\|_2$ separately:

Proposition 3.1 (Naive bound). *Let $\|x_i\|_2 \leq B_X$ for all tokens. Then:*

$$\max_{i,j} |S_{ij}| \leq \frac{\|W^Q\|_2 \|W^K\|_2 \cdot B_X^2}{\sqrt{d_h}}. \quad (5)$$

This bound is loose because it treats W^Q and W^K independently. Analyzing $M = W^Q W^{K^\top}$ directly yields a tighter result:

Proposition 3.2 (Interaction bound). *Under the same conditions:*

$$\max_{i,j} |S_{ij}| \leq \frac{\|W^Q W^{K^\top}\|_2 \cdot B_X^2}{\sqrt{d_h}}. \quad (6)$$

Corollary 3.3 (Interaction bound is tighter). $\|W^Q W^{K^\top}\|_2 \leq \|W^Q\|_2 \|W^K\|_2$, with equality iff the top right singular vectors of W^Q and W^K coincide.

For pre-LN architectures (GPT-2, Llama, Mistral), LayerNorm or RMSNorm (Zhang & Sennrich, 2019) precedes attention, constraining $\|x_i\|_2^2 \approx d$ and giving $B_X = \sqrt{d}$. Substituting yields the *worst-case bound*:

$$\max_{i,j} |S_{ij}| \leq \|W^Q W^{K^\top}\|_2 \cdot \frac{d}{\sqrt{d_h}} =: B_{\max}. \quad (7)$$

Calibrating the bound. The bound B_{\max} assumes input vectors align perfectly with the top singular vectors of M .

In practice, this is overly pessimistic: the worst case requires inputs to find the direction of maximum amplification in a d -dimensional space, but LayerNorm-normalized inputs behave like random directions on the sphere. In high dimensions, random vectors are nearly orthogonal to any fixed direction, making such alignment exponentially unlikely.

This concentration phenomenon motivates introducing a calibration factor $\alpha \in (0, 1)$. The *calibrated bound* is:

$$B_\alpha := \alpha \cdot B_{\max} = \alpha \cdot \|M\|_2 \cdot \frac{d}{\sqrt{d_h}}. \quad (8)$$

Smaller α yields a tighter bound and higher FP8 dynamic range utilization, but increases the probability that actual logits exceed the bound. The natural question is how to select α : small enough to be practical, yet large enough to guarantee safety. In the next section, we develop a probabilistic framework that provides a principled answer.

3.2. Rank-Aware Probabilistic Guarantee

We derive a probabilistic bound on $\Pr(\max_{i,j} |S_{ij}| \geq B_\alpha)$ that enables principled selection of the calibration factor α . Proofs for this section are in Appendix B.

Assumption (Spherical token directions). For Pre-LN transformers, we model post-LayerNorm (or post-RMSNorm) token vectors as $x_i = \sqrt{d}u_i$, where directions u_i are approximately isotropic (idealized as i.i.d. uniform on \mathbb{S}^{d-1}). For self-attention, where queries and keys derive from the same tokens, we treat each role’s projection direction as an independent draw. This assumption captures the effect of normalization in high dimensions and is the *only* distributional assumption required for Proposition 3.4.

Remark (Diagonal terms). For diagonal terms ($i = j$), the attention score involves the quadratic form $u_i^\top M u_i$ rather than a bilinear form with independent arguments. Our analysis treats these as bilinear by assuming independence. This is conservative for two reasons: (i) diagonal terms constitute only L of L^2 query-key pairs, a vanishing fraction as L grows; and (ii) quadratic forms $u^\top M u$ for u uniform on the sphere exhibit *tighter* concentration than bilinear forms $u^\top M v$ with independent u, v (the variance is smaller when both vectors are identical). Thus, the independence assumption yields an upper bound on overflow probability.

Under this model, and exploiting the low-rank structure of the query-key interaction matrix $\text{rank}(M) \leq d_h \ll d$, we obtain a tail bound whose concentration exponent improves by a factor of $d/(\gamma d_h)$ over rank-agnostic arguments. Table 2 quantifies this improvement for representative architectures (see Appendix B.3 for derivation details).

Our goal is a safety guarantee covering all tokens, heads,

Table 2. Concentration exponent improvement from rank-aware bounds: $d/(\gamma d_h)$ tighter tail probabilities, where γ is determined by Eq. (12).

Model	d	d_h	γ	Improvement
GPT-2 XL	1600	64	2.98	8×
Mistral-7B	4096	128	2.26	14×
Llama-2-13B	5120	128	2.28	18×
Llama-2-70B	8192	128	2.32	28×

and layers. Accordingly, the analysis applies union bounds over L^2 query-key pairs and over all attention heads. This yields a conservative bound that remains robust under transient conditions (e.g., checkpoint loading and learning-rate discontinuities), while leaving slack in typical steady-state regimes.

Proposition 3.4 (Rank-aware overflow probability bound). Let $M = W^Q W^{K\top}$ with $W^Q, W^K \in \mathbb{R}^{d \times d_h}$ for a single attention head and $\text{rank}(M) = d_h$. For a sequence of length L and any $\gamma > 1$,

$$\text{where } \Pr(\max_{i,j} |S_{ij}| \geq B_\alpha) \leq T_1 + T_2, \quad (9)$$

$$T_1 = L \exp\left(-\frac{d_h}{2}(\gamma - 1 - \ln \gamma)\right), \quad (10)$$

$$T_2 = 2L^2 \exp\left(-\frac{d^2 \alpha^2}{2\gamma d_h}\right). \quad (11)$$

The term T_1 bounds the probability that any key projection is atypically large, while T_2 bounds overflow conditioned on typical key projections. The parameter $\gamma > 1$ controls the typicality threshold.

Extension to full transformers. Proposition 3.4 bounds overflow probability for a single attention head. For a transformer with $N = n_{\text{layers}} \times n_{\text{heads}}$ heads, overflow occurs if *any* head overflows. Applying a union bound,

$$\Pr(\text{overflow in any head}) \leq N(T_1 + T_2).$$

To ensure this probability is at most δ^* , it suffices to require $N \cdot T_1 \leq \delta^*/2$ and $N \cdot T_2 \leq \delta^*/2$.² Solving these inequalities yields a principled selection rule for γ and α .

Principled α selection. Step 1: Select γ . From $N \cdot T_1 \leq \delta^*/2$ and (10), we require

$$h(\gamma) := \gamma - 1 - \ln \gamma \geq \frac{2}{d_h} \ln\left(\frac{2NL}{\delta^*}\right). \quad (12)$$

Step 2: Select α . From $N \cdot T_2 \leq \delta^*/2$ and (11), we require

$$\alpha \geq \alpha_{\min} := \frac{\sqrt{2\gamma d_h}}{d} \sqrt{\ln\left(\frac{4NL^2}{\delta^*}\right)}. \quad (13)$$

Table 3 reports α_{\min} for our evaluated models with $\delta^* = 10^{-6}$ and $L = 1024$.

²The equal allocation is a standard simplification; optimizing the split yields negligible improvement in practice.

Table 3. Minimum calibration factor α_{\min} for $\delta^* = 10^{-6}$ and $L = 1024$.

Model	d	d_h	N	α_{\min}
GPT-2 XL	1600	64	1200	0.074
Mistral-7B	4096	128	1024	0.035
Llama-2-13B	5120	128	1600	0.028
Llama-2-70B	8192	128	5120	0.018

Selecting α in practice. We set α slightly above α_{\min} for safety margin. Larger models permit smaller α due to stronger concentration arising from higher $d/\sqrt{d_h}$ ratios. In our experiments, we use $\alpha = 0.08$ for GPT-2 XL, $\alpha = 0.04$ for Mistral-7B, $\alpha = 0.03$ for Llama-2-13B, and $\alpha = 0.02$ for Llama-2-70B, each exceeding the corresponding α_{\min} .

Transient vs. steady-state regimes. Eq. (13) yields a conservative α_{\min} designed for transient-prone workflows (pre-trained loading, checkpoint resumption without FP8 state, and LR discontinuities) where a single overflow can corrupt training. For steady-state fine-tuning, we optionally tighten α using a one-time empirical calibration (Sec. 3.5), then freeze it and revert to fully predictive scaling.

Modern architectures (Llama, Mistral) use Rotary Position Embeddings (RoPE), which apply position-dependent rotations to query and key vectors. We show our bounds extend without modification.

3.3. Extension to Rotary Position Embeddings

Rotary Position Embeddings (Su et al., 2021) apply rotation matrices to query and key vectors before computing attention:

$$S_{mn} = \frac{(R_m q_m)^\top (R_n k_n)}{\sqrt{d_h}} = \frac{q_m^\top R_m^\top R_n k_n}{\sqrt{d_h}}, \quad (14)$$

where $R_m, R_n \in \mathbb{R}^{d_h \times d_h}$ are position-dependent block-diagonal rotation matrices. The following results, proved in Appendix C, show these rotations cannot amplify scores beyond our bounds.

Proposition 3.5 (RoPE preserves norms). *Let $R_\theta \in \mathbb{R}^{d_h \times d_h}$ be any RoPE rotation matrix. Then:*

1. R_θ is orthogonal: $R_\theta^\top R_\theta = I$.
2. $\|R_\theta\|_2 = 1$.
3. For any $q, k \in \mathbb{R}^{d_h}$: $|(R_m q)^\top (R_n k)| \leq \|q\| \cdot \|k\|$.

Corollary 3.6 (Geometry-aware scaling extends to RoPE). *For RoPE-based attention, the worst-case bound $|S_{mn}| \leq \|W^Q\|_2 \|W^K\|_2 \cdot d/\sqrt{d_h}$ holds rigorously for all positions via $\|R_m\|_2 = 1$. The tighter interaction bound $\|W^Q W^{K^\top}\|_2$ applies when RoPE rotations do not systematically align with the singular subspaces of W^Q and*

W^K , a condition we verified empirically across all layers in Mistral-7B, Llama-2-13B, and Llama-2-70B.

The probabilistic bound (Proposition 3.4) also extends conservatively; see Appendix C.4.

3.4. Geometry-Aware Scale Factor

Spectral norms vary by up to $10\times$ across layers (Appendix D), so a global scale would severely underutilize FP8 precision. We therefore compute scale factors per layer.

For layer ℓ , let $\sigma_{QK}^{(\ell)} = \|W_{(\ell)}^Q W_{(\ell)}^{K^\top}\|_2$ denote the spectral norm of the interaction matrix. The calibrated bound for layer ℓ is:

$$B_\alpha^{(\ell)} = \alpha \cdot \sigma_{QK}^{(\ell)} \cdot \frac{d}{\sqrt{d_h}}.$$

To map this bound to a scale factor, we define $R_{\text{safe}} = \eta_{\text{fp8}} \cdot 448$, where $\eta_{\text{fp8}} < 1$ provides margin below the E4M3 maximum. The geometry-aware scale factor is:

$$\text{scale}^{(\ell)} = \frac{B_\alpha^{(\ell)}}{R_{\text{safe}}} = \frac{\alpha \cdot \sigma_{QK}^{(\ell)} \cdot d/\sqrt{d_h}}{\eta_{\text{fp8}} \cdot 448}. \quad (15)$$

During the forward pass, pre-softmax attention scores $S^{(\ell)} = Q^{(\ell)} K^{(\ell)\top} / \sqrt{d_h}$ are divided by $\text{scale}^{(\ell)}$ before FP8 quantization, ensuring scaled logits lie within the representable range. In all experiments, we set $\eta_{\text{fp8}} = 0.8$ and select α per model following Section 3.2.

For architectures with grouped query attention (GQA), where multiple query heads share key-value heads, we compute $\sigma_{QK}^{(\ell)}$ without expanding the key matrix; this implicit formulation is described in Section 4.2.

3.5. Auto- α Calibration for Steady-State Training

The conservative α from Proposition 3.4 guarantees overflow probability below $\delta^* = 10^{-6}$, appropriate for transient-prone workflows. However, during steady-state fine-tuning, actual logits occupy a small fraction of the theoretical envelope. Auto- α is an *optional* enhancement for practitioners who prioritize utilization over worst-case robustness.

We define the *slack ratio* at step t as:

$$r_t = \frac{\max_{i,j} |S_{ij}^{(t)}|}{B_{\max}}, \quad (16)$$

where the numerator is the observed maximum logit.

Algorithm. Auto- α calibration proceeds in two phases:

1. **Burn-in** (steps 1 to T_{calib}): Run with conservative α_0 from Proposition 3.4. Collect slack ratios $\{r_t\}$.

2. **Calibration:** Set $\alpha_{\text{final}} = P_{99.99}(\{r_t\}) \times \kappa$, where $\kappa \geq 1$ is a safety multiplier.

The calibrated α_{final} is then frozen for all subsequent training. This is distinct from delayed scaling: we measure slack to select a *static* bound, not to continuously adapt. After burn-in, the method is again fully predictive.

Theoretical guarantee. When using auto- α , the probabilistic guarantee from Proposition 3.4 no longer applies, since the calibration factor is determined empirically rather than from the theoretical selection rule (Eq. 13). Auto- α trades the worst-case guarantee for higher utilization, relying on the assumption that the burn-in distribution is representative of subsequent training. This is appropriate for steady-state fine-tuning but not for workflows with anticipated distribution shifts.

Memory-efficient attention compatibility. Auto- α calibration requires observing $\max_{i,j} |S_{ij}|$ during the burn-in phase, which necessitates materializing the score matrix and is incompatible with FlashAttention. For a 100-step burn-in out of thousands of training steps, this overhead is negligible ($< 0.1\%$ of total compute). After burn-in, the calibrated α is frozen and the method reverts to fully predictive scaling compatible with memory-efficient attention.

4. Efficient Estimation of Spectral Bounds

This section presents efficient algorithms for computing the spectral bounds.

4.1. Spectral Norm Estimation via Power Iteration

Computing $\|M\|_2$ where $M = W^Q W^{K\top} \in \mathbb{R}^{d \times d}$ via full SVD costs $O(d^3)$, which is prohibitive for large models. For Llama-2-70B with $d = 8192$, this would require forming a 67 million entry matrix per layer.

We instead use power iteration (Golub & Van Loan, 2013), a classical algorithm that estimates the top singular value through repeated matrix-vector multiplication. The key insight is that we never form M explicitly. Starting from random unit vectors $u, v \in \mathbb{R}^d$, we alternate:

$$u \leftarrow \frac{Mv}{\|Mv\|}, \quad \text{then} \quad v \leftarrow \frac{M^\top u}{\|M^\top u\|}. \quad (17)$$

After these updates, $\|Mv\|$ provides an estimate of $\|M\|_2$. Each matrix-vector product is computed implicitly:

$$Mv = W^Q (W^{K\top} v), \quad (18)$$

$$M^\top u = W^K (W^{Q\top} u), \quad (19)$$

requiring $O(n_{\text{heads}} \cdot d_h \cdot d)$ operations per iteration, where n_{heads} is the total number of attention heads. This is far

cheaper than explicitly forming $M \in \mathbb{R}^{d \times d}$, which would require $O(n_{\text{heads}} \cdot d_h \cdot d^2)$ operations and $O(d^2)$ memory.

We maintain the persistent vectors u, v across training steps. During steady-state training, weights change gradually (controlled by the learning rate), so singular vectors drift slowly and one iteration per forward pass suffices to track them. For cold-start scenarios (initialization, checkpoint loading), we run 5 iterations to ensure convergence from random vectors.

Remark (Transient robustness). Even during rapid weight changes (e.g., learning rate spikes), any underestimation of the spectral norm is bounded. If the true spectral norm increases by factor ρ from step t to $t + 1$, power iteration with warm-start vectors underestimates by at most ρ until the next update. Since our calibration factor α already provides margin above α_{min} (Section 3.2), moderate underestimation does not cause overflow. Our experiments with $100\times$ learning rate spikes (Section 5.2) confirm zero overflows under this regime.

The detailed algorithm is provided in Appendix E.

4.2. Implicit Formulation for Grouped Query Attention

Modern architectures use Grouped Query Attention (GQA) (Ainslie et al., 2023), where multiple query heads share key-value heads. For example, Mistral-7B has $n_q = 32$ query heads but only $n_{kv} = 8$ key-value heads (a 4:1 ratio). This creates a dimension mismatch: $W^Q \in \mathbb{R}^{d \times (n_q \cdot d_h)}$ while $W^K \in \mathbb{R}^{d \times (n_{kv} \cdot d_h)}$.

To compute $\|W^Q W^{K\top}\|_2$ with matching dimensions, a naive approach would expand W^K by replicating each block of d_h columns $g = n_q/n_{kv}$ times to form $W_{\text{exp}}^K \in \mathbb{R}^{d \times (n_q \cdot d_h)}$. This expansion consumes substantial memory: 32MB per layer on Mistral-7B.

We observe that power iteration requires only matrix-vector products, not the matrices themselves. For the forward product Mv where $M = W^Q W_{\text{exp}}^{K\top}$:

$$Mv = W^Q \cdot \text{REPEATBLOCKS}(W^{K\top} v, g),$$

where $\text{REPEATBLOCKS}(z, g)$ replicates each d_h -block of $z \in \mathbb{R}^{n_{kv} \cdot d_h}$ exactly g times to produce a vector in $\mathbb{R}^{n_q \cdot d_h}$. The reverse product $M^\top u$ uses a dual operation: $M^\top u = W^K \cdot \text{SUMGROUPS}(W^{Q\top} u, g)$, where SUMGROUPS sums each group of g blocks. These operations require replicating only small intermediate vectors ($n_{kv} \cdot d_h$ elements) rather than the full weight matrix.

Proposition 4.1 (Implicit GQA power iteration). *Power iteration using the unexpanded W^K converges to the same spectral norm $\|W^Q W_{\text{exp}}^{K\top}\|_2$ as explicit expansion.*

The proof and detailed algorithm are in Appendix F. By avoiding the expanded matrix, we reduce memory transac-

tions by a factor of g ($4\text{--}8\times$ on modern GQA architectures). This saving can offset the cost of power iteration, yielding negligible or even negative overhead in practice (Table 9).

4.3. Complete Algorithm

Algorithm 1 presents the complete forward pass. The algorithm is *predictive* (scale depends only on weights), *fused-compatible* (no activation observation), and *per-layer*.

Algorithm 1 Geometry-Aware Attention Forward Pass

- 1: **Input:** Token embeddings $X \in \mathbb{R}^{L \times d}$, layer weights W^Q, W^K, W^V, W^O
 - 2: **Parameters:** Calibration factor α , FP8 margin η_{fp8}
 - 3: **State:** Persistent vectors u, v for power iteration
 - 4:
 - 5: {Stage 1: Estimate spectral norm from weights}
 - 6: $\sigma_{QK} \leftarrow \text{POWERITERATION}(W^Q, W^K, u, v)$
 - 7:
 - 8: {Stage 2: Compute predictive scale factor}
 - 9: $B_\alpha \leftarrow \alpha \cdot \sigma_{QK} \cdot d / \sqrt{d_h}$
 - 10: $\text{scale} \leftarrow B_\alpha / (\eta_{\text{fp8}} \cdot 448)$
 - 11:
 - 12: {Stage 3: Attention with pre-computed scale}
 - 13: $Q, K, V \leftarrow XW^Q, XW^K, XW^V$
 - 14: $S \leftarrow QK^\top / \sqrt{d_h}$
 - 15: $\tilde{S} \leftarrow S / \text{scale}$
 - 16: **return** $\text{softmax}(\tilde{S}) \cdot V \cdot W^O$
-

5. Experiments

We evaluate geometry-aware scaling across four transformer architectures spanning 1.5B to 70B parameters. Our experiments address three questions: (1) Does geometry-aware scaling eliminate overflows in transient scenarios where delayed scaling fails? (2) Does the safety–utilization tradeoff affect downstream task quality? (3) What is the computational cost?

The key property enabling transient safety is that geometry-aware scaling responds instantaneously to weight changes: the scale factor is computed from current weights, not historical activations. Appendix H validates this with a controlled experiment where we spike attention weights by $4\times$; delayed scaling overflows catastrophically while geometry-aware scaling adapts in the same forward pass. The following sections demonstrate that this instantaneous response eliminates overflow in realistic training scenarios.

5.1. Experimental Setup

Models. We evaluate on four models: GPT-2 XL (1.5B parameters, 48 layers), Mistral-7B (32 layers), Llama-2-13B (40 layers), and Llama-2-70B (80 layers). The models include both standard multi-head attention (GPT-2 XL, Llama-2-13B) and grouped query attention (Mistral-7B with 4:1

ratio, Llama-2-70B with 8:1 ratio), enabling evaluation of the implicit GQA formulation. Architectural specifications and hardware details are in Appendix G.1.

Implementation details. All experiments use FP8 E4M3 format with margin $\eta_{\text{fp8}} = 0.8$, giving a safe range of $0.8 \times 448 = 358.4$. Calibration factors are set per model following the procedure in Section 3.2: $\alpha = 0.08$ for GPT-2 XL, 0.04 for Mistral-7B, 0.03 for Llama-2-13B, and 0.02 for Llama-2-70B. Power iteration uses persistent vectors with one update per forward pass; we initialize with 5 iterations at the start of training or after checkpoint loading to ensure convergence from random initialization.

5.2. Transient Scenarios

We evaluate three transient scenarios that expose the history staleness problem in delayed scaling.

Loading pretrained models. The most common scenario is loading pretrained weights into an FP8 training pipeline. The history buffer initializes to default values while weights reflect extensive prior training, creating immediate mismatch.

Table 4 shows overflow statistics on the first forward pass after loading pretrained weights. Delayed scaling overflows on 100% of layers across all four models, with maximum scaled logits exceeding 5000. Geometry-aware scaling achieves zero overflows because the scale factor is computed directly from the loaded weights in the same forward pass.

Table 4. First forward pass after loading pretrained weights. **Overflow:** layers exceeding 448. **Max Scaled:** maximum scaled logit.

Model	Delayed		Ours	
	Overfl.	Max Scaled	Overfl.	Max Scaled
GPT-2 XL	48/48	8761	0/48	120
Mistral-7B	32/32	7123	0/32	196
Llama-2-13B	40/40	5600	0/40	2.5
Llama-2-70B	80/80	9498	0/80	1.0

Checkpoint resumption. Training large models involves interruptions due to job preemption, hardware failures, or scheduled maintenance. Upon resumption, the history buffer resets to default values while model weights reflect the training state at the checkpoint.

We simulate this by training for 300 steps, saving a checkpoint, then resuming with a fresh history buffer. In the first 10 steps after resumption, delayed scaling overflows on 4 steps for GPT-2 XL, 2 steps for Llama-2-70B, and 1 step each for Mistral-7B and Llama-2-13B. Geometry-aware scaling maintains zero overflows across all models because the scale factor depends only on current weights, which are

restored correctly from the checkpoint. While checkpointing scaling state is possible, standard frameworks do not include it by default, and loading pretrained weights from external sources provides no history at all.

Learning rate transitions. Learning rate schedules involve sudden changes: warmup phases ramp the rate over initial steps, and cyclic schedules spike periodically. These transitions cause weights to change faster than the history buffer can track.

We evaluate with a $100\times$ spike: learning rate 10^{-5} for 100 steps, then 10^{-3} . In the 10 steps following the transition, delayed scaling overflows on 3 to 5 steps depending on the model (5 for Mistral-7B, 4 for Llama-2-70B, 3 for Llama-2-13B). On GPT-2 XL, NaN gradients appear immediately, terminating training. Geometry-aware scaling handles the transition with zero overflows across all models.

5.3. Computational Overhead

Geometry-aware scaling requires computing spectral norms via power iteration, adding computational cost. We measure forward pass timing averaged over 100 iterations (detailed methodology in Appendix I). On MHA architectures, overhead is minimal: +1.0% for GPT-2 XL and +1.9% for Llama-2-13B. On Mistral-7B with GQA (4:1 ratio), we observe *negative* overhead of -5.3%: geometry-aware scaling is faster than delayed scaling in our implementation. We attribute this to our implicit GQA formulation (Section 4.2), which has favorable memory access patterns, combined with synchronization overhead in the baseline’s history buffer updates. However, this result is implementation-specific; the key finding is that overhead is negligible across all architectures. Llama-2-70B shows +4.3% due to its 80 layers; full details in Appendix I.

5.4. Downstream Task Evaluation

Training loss measures average next-token prediction but may mask degradation in reasoning. We evaluate on MMLU (Hendrycks et al., 2021) to verify that geometry-aware scaling preserves downstream capability. We fine-tune Llama-2-13B for 3000 steps on MMLU STEM subjects (17 subjects, 295 training examples) using three methods: delayed scaling, conservative spectral scaling ($\alpha = 0.03$), and auto- α spectral scaling (100-step burn-in, $\kappa = 1.0$). All methods use identical hyperparameters: learning rate 10^{-5} , batch size 4, sequence length 1024. We evaluate on held-out test sets (2783 examples).

Table 5 shows training metrics and downstream accuracy. All three methods converge to similar training loss (≈ 0.012), yet downstream accuracy differs substantially. Conservative spectral scaling achieves zero overflows but degrades accuracy by 5 percentage points (28.1% vs. 33.0%),

indicating that 0.5% FP8 utilization introduces excessive quantization noise, losing fine-grained distinctions between attention logits even when average loss remains low. Auto- α calibration resolves this tradeoff: by tightening α from 0.03 to 0.00036 based on the 99.99th percentile of observed slack ratios, utilization increases to 31.2%, achieving comparable accuracy (33.6%) while maintaining zero overflows.

Caveats. The primary contribution of this evaluation is demonstrating that geometry-aware scaling *eliminates overflows* without catastrophic accuracy degradation, not that it improves accuracy over the baseline. The 0.6 percentage point difference between auto- α (33.6%) and delayed scaling (33.0%) is within the variance expected from stochastic optimization on a small training set (295 examples); we do not claim statistical significance for this difference. For the delayed scaling baseline, overflows (68 occurrences) were handled by clamping to the representable range, allowing training to continue; without clamping, NaN propagation would terminate training entirely.

Table 5. Training metrics and MMLU STEM accuracy on Llama-2-13B. Auto- α achieves comparable accuracy to the baseline while eliminating all overflows.

Method	Loss	Overfl.	Util.	MMLU
Delayed	0.0116	68	70.7%	33.0%
Ours (conservative)	0.0119	0	0.5%	28.1%
Ours + auto-α	0.0116	0	31.2%	33.6%

These results suggest a practical workflow: conservative α for transient-prone scenarios (checkpoint loading, learning rate warmup) where safety is paramount, and auto- α for steady-state fine-tuning where utilization matters. Training loss curves are provided in Appendix K, per-subject accuracy in Appendix L, and FP8 utilization statistics in Appendix J.

6. Conclusion

We established spectral bounds on transformer attention logits and derived a rank-aware probabilistic calibration framework for low-precision training. The key theoretical result is $\max_{i,j} |S_{ij}| \leq \|W^Q W^{K\top}\|_2 \cdot d/\sqrt{d_n}$, which is never looser than the naive submultiplicative bound and is strictly tighter unless the top right singular vectors of W^Q and W^K align. This bound, combined with our rank-aware probabilistic analysis, provides principled calibration given a target failure probability δ^* . The bound is efficiently computable via power iteration and extends conservatively to RoPE architectures. Experiments demonstrate zero overflows across GPT-2 XL through Llama-2-70B on all transient scenarios where delayed scaling fails, with negligible computational overhead. Auto- α calibration resolves the utilization-accuracy trade-off: by learning a data-driven bound during burn-in, we achieve comparable MMLU accuracy to delayed scaling while eliminating all overflows.

Impact Statement

This work improves reliability and efficiency of FP8 training; we do not anticipate ethical risks beyond those inherent to large-scale ML training.

References

- Ainslie, J., Lee-Thorp, J., de Jong, M., Zemlyanskiy, Y., Lebrón, F., and Sanghai, S. GQA: Training generalized multi-query transformer models from multi-head checkpoints. In *Proceedings of the 2023 Conference on Empirical Methods in Natural Language Processing*, pp. 4895–4901. Association for Computational Linguistics, 2023.
- Blake, C., Orr, D., and Luschi, C. Unit scaling: Out-of-the-box low-precision training. In *Proceedings of the 40th International Conference on Machine Learning*, volume 202 of *Proceedings of Machine Learning Research*, pp. 2548–2576. PMLR, 2023.
- Choi, K., Lee, H., Park, S., Kwon, D., and Lee, J. FALQON: Accelerating LoRA fine-tuning with low-bit floating-point arithmetic. In *Advances in Neural Information Processing Systems*, volume 38, 2025.
- Dao, T. FlashAttention-2: Faster attention with better parallelism and work partitioning. In *International Conference on Learning Representations*, 2024.
- Dao, T., Fu, D. Y., Ermon, S., Rudra, A., and Ré, C. FlashAttention: Fast and memory-efficient exact attention with IO-awareness. In *Advances in Neural Information Processing Systems*, volume 35, pp. 16344–16359, 2022.
- DeepSeek-AI. Deepseek-v3 technical report. *arXiv preprint arXiv:2412.19437*, 2024.
- Golub, G. H. and Van Loan, C. F. *Matrix Computations*. Johns Hopkins University Press, 4th edition, 2013.
- Hendrycks, D., Burns, C., Basart, S., Zou, A., Mazeika, M., Song, D., and Steinhardt, J. Measuring massive multitask language understanding. In *International Conference on Learning Representations*, 2021.
- Hernández-Cano, A., Garbaya, D., Schlag, I., and Jaggi, M. Towards fully FP8 GEMM LLM training at scale. In *Advances in Neural Information Processing Systems*, volume 38, 2025.
- Laurent, B. and Massart, P. Adaptive estimation of a quadratic functional by model selection. *Annals of Statistics*, 28(5):1302–1338, 2000.
- Lee, H., Kwon, O., Park, Y., and Lee, J. W. NestedFP: High-performance, memory-efficient dual-precision floating point support for LLMs. In *Advances in Neural Information Processing Systems*, volume 38, 2025.
- Micikevicius, P., Stosic, D., Burgess, N., Cornea, M., Dubey, P., Grisenthwaite, R., Ha, S., Heinecke, A., Judd, P., Kamalu, J., et al. FP8 formats for deep learning. *arXiv preprint arXiv:2209.05433*, 2022.
- Miyato, T., Kataoka, T., Koyama, M., and Yoshida, Y. Spectral normalization for generative adversarial networks. In *International Conference on Learning Representations*, 2018. URL <https://openreview.net/forum?id=B1QRgziT->.
- Rouhani, B. D., Zhao, R., Elango, V., Shafipour, R., Rouhani, M. D., et al. Microscaling data formats for deep learning. *arXiv preprint arXiv:2310.10537*, 2023.
- Shah, J., Bikshandi, G., Zhang, Y., Thakkar, V., Ramani, P., and Dao, T. Flashattention-3: Fast and accurate attention with asynchrony and low-precision. In *Advances in Neural Information Processing Systems*, volume 37, 2024.
- Su, J., Lu, Y., Pan, S., Murtadha, A., Wen, B., and Liu, Y. RoFormer: Enhanced transformer with rotary position embedding. *arXiv preprint arXiv:2104.09864*, 2021.
- Zhai, S., Likhomanenko, T., Littwin, E., Busbridge, D., Ramapuram, J., Zhang, Y., Gu, J., and Susskind, J. M. Stabilizing Transformer training by preventing attention entropy collapse. In *Proceedings of the 40th International Conference on Machine Learning*, pp. 40770–40803. PMLR, 2023.
- Zhang, B. and Sennrich, R. Root mean square layer normalization. In *Advances in Neural Information Processing Systems*, volume 32, 2019.
- Zhang, Y., Zhen, H.-L., Yuan, M., and Yu, B. MOSS: Efficient and accurate FP8 LLM training with microscaling and automatic scaling. *arXiv preprint arXiv:2511.05811*, 2025.

A. Proofs for Section 3.1

This appendix contains the proofs for propositions and corollaries stated in Section 3.1.

A.1. Proof of Proposition 3.1 (Naive Bound)

Proof. By the Cauchy-Schwarz inequality:

$$|S_{ij}| = \frac{|q_i^\top k_j|}{\sqrt{d_h}} \leq \frac{\|q_i\|_2 \|k_j\|_2}{\sqrt{d_h}}.$$

Since $q_i = W^{Q\top} x_i$ and $k_j = W^{K\top} x_j$, submultiplicativity of the spectral norm gives:

$$\|q_i\|_2 = \|W^{Q\top} x_i\|_2 \leq \|W^{Q\top}\|_2 \|x_i\|_2 = \|W^Q\|_2 B_X,$$

and similarly $\|k_j\|_2 \leq \|W^K\|_2 B_X$. Combining these:

$$|S_{ij}| \leq \frac{\|W^Q\|_2 \|W^K\|_2 \cdot B_X^2}{\sqrt{d_h}}. \quad \square$$

A.2. Proof of Proposition 3.2 (Interaction Bound)

Proof. Define $M = W^Q W^{K\top} \in \mathbb{R}^{d \times d}$. The attention score can be written as a bilinear form:

$$S_{ij} = \frac{x_i^\top W^Q W^{K\top} x_j}{\sqrt{d_h}} = \frac{x_i^\top M x_j}{\sqrt{d_h}}.$$

By the variational characterization of the spectral norm:

$$\|M\|_2 = \max_{\|u\|_2 = \|v\|_2 = 1} |u^\top M v|.$$

Therefore, for any vectors x_i, x_j :

$$|x_i^\top M x_j| \leq \|M\|_2 \cdot \|x_i\|_2 \cdot \|x_j\|_2 \leq \|M\|_2 \cdot B_X^2,$$

which gives $|S_{ij}| \leq \|M\|_2 \cdot B_X^2 / \sqrt{d_h}$. \square

A.3. Proof of Corollary 3.3 (Interaction Bound is Tighter)

Proof. The inequality $\|W^Q W^{K\top}\|_2 \leq \|W^Q\|_2 \|W^K\|_2$ follows directly from submultiplicativity of the spectral norm: for any matrices A, B of compatible dimensions, $\|AB\|_2 \leq \|A\|_2 \|B\|_2$.

For the equality condition, let $W^Q = U_Q \Sigma_Q V_Q^\top$ and $W^K = U_K \Sigma_K V_K^\top$ be the singular value decompositions. Then:

$$W^Q W^{K\top} = U_Q \Sigma_Q V_Q^\top V_K \Sigma_K U_K^\top.$$

The spectral norm of this product equals $\sigma_1(W^Q) \cdot \sigma_1(W^K)$ if and only if the $(1, 1)$ entry of $V_Q^\top V_K$ has absolute value 1, which requires the top right singular vectors to coincide: $v_1^Q = \pm v_1^K$.

Under random initialization, singular vectors are uniformly distributed on the sphere, making exact alignment a measure-zero event. \square

B. Proofs for Section 3.2

This appendix contains the proofs for Proposition 3.4, as well as supporting lemmas.

B.1. Supporting Lemmas

We first establish a tail bound for the projection of a uniform random vector onto a subspace.

Lemma B.1 (Projection norm distribution). *Let $u \sim \text{Unif}(\mathbb{S}^{d-1})$ and let $V \in \mathbb{R}^{d \times k}$ have orthonormal columns spanning a k -dimensional subspace. Then:*

$$\|V^\top u\|_2^2 \sim \text{Beta}\left(\frac{k}{2}, \frac{d-k}{2}\right), \quad \mathbb{E}[\|V^\top u\|_2^2] = \frac{k}{d}.$$

Proof. The uniform distribution on \mathbb{S}^{d-1} can be generated as $u = g/\|g\|_2$ where $g \sim \mathcal{N}(0, I_d)$. Since V has orthonormal columns, $V^\top g \sim \mathcal{N}(0, I_k)$, and let $V_\perp \in \mathbb{R}^{d \times (d-k)}$ complete an orthonormal basis, so $V_\perp^\top g \sim \mathcal{N}(0, I_{d-k})$ independently.

Then $\|V^\top g\|_2^2 \sim \chi_k^2$ and $\|V_\perp^\top g\|_2^2 \sim \chi_{d-k}^2$ are independent, and:

$$\|V^\top u\|_2^2 = \frac{\|V^\top g\|_2^2}{\|g\|_2^2} = \frac{\|V^\top g\|_2^2}{\|V^\top g\|_2^2 + \|V_\perp^\top g\|_2^2}.$$

The ratio of independent chi-squared variables $\chi_k^2/(\chi_k^2 + \chi_{d-k}^2)$ follows $\text{Beta}(k/2, (d-k)/2)$. \square

Lemma B.2 (Chi-squared ratio tail bound). *Let $X \sim \text{Beta}(k/2, (d-k)/2)$. For any $\gamma > 1$:*

$$\Pr\left(X \geq \gamma \cdot \frac{k}{d}\right) \leq \exp\left(-\frac{k}{2}(\gamma - 1 - \ln \gamma)\right).$$

Proof. By Lemma B.1, $X \sim \text{Beta}(k/2, (d-k)/2)$ with mean $\mu = k/d$. The stated bound follows from the multiplicative Chernoff bound for Beta distributions.

For $X \sim \text{Beta}(a, b)$ and $\gamma > 1$, the moment generating function yields:

$$\Pr\left(X \geq \gamma \cdot \frac{a}{a+b}\right) \leq \exp(-a \cdot h(\gamma)),$$

where $h(\gamma) = \gamma - 1 - \ln \gamma > 0$ for $\gamma > 1$. This is the Beta analogue of the chi-squared Chernoff bound (Laurent & Massart, 2000, Lemma 1) and follows from the representation of Beta as a ratio of independent Gamma variables.

Setting $a = k/2$ and noting that $a/(a+b) = k/d$:

$$\Pr\left(X \geq \gamma \cdot \frac{k}{d}\right) \leq \exp\left(-\frac{k}{2}(\gamma - 1 - \ln \gamma)\right). \quad \square$$

B.2. Proof of Proposition 3.4 (Rank-Aware Overflow Bound)

Proof. Under the spherical assumption, token vectors satisfy $x_i = \sqrt{d} \cdot u_i$ where $u_i \sim \text{Unif}(\mathbb{S}^{d-1})$ independently. The attention score becomes:

$$S_{ij} = \frac{d}{\sqrt{d_h}} \cdot u_i^\top M u_j,$$

and the calibrated bound is $B_\alpha = \alpha \cdot \|M\|_2 \cdot d/\sqrt{d_h}$. We must bound:

$$\Pr\left(\max_{i,j} |S_{ij}| \geq B_\alpha\right) = \Pr\left(\max_{i,j} |u_i^\top M u_j| \geq \alpha \|M\|_2\right).$$

Step 1: SVD decomposition. Let $M = U\Sigma V^\top$ be the SVD with $\text{rank}(M) = d_h$, where $V \in \mathbb{R}^{d \times d_h}$ contains the right singular vectors. For any unit vector u_j :

$$M u_j = U\Sigma V^\top u_j,$$

$$\text{so } \|M u_j\|_2 = \|\Sigma V^\top u_j\|_2 \leq \sigma_1 \|V^\top u_j\|_2 = \|M\|_2 \|V^\top u_j\|_2.$$

Step 2: Define typical keys. For $\gamma > 1$, define the typical key event:

$$\mathcal{E}_j := \left\{ \|V^\top u_j\|_2^2 \leq \gamma \cdot \frac{d_h}{d} \right\},$$

which implies $\|M u_j\|_2 \leq \|M\|_2 \sqrt{\gamma d_h/d} =: \beta \|M\|_2$ where $\beta = \sqrt{\gamma d_h/d}$.

Let $\mathcal{E} = \bigcap_{j=1}^L \mathcal{E}_j$ be the event that all keys are typical.

Step 3: Bound probability of atypical keys. By Lemmas B.1 and B.2:

$$\begin{aligned} \Pr(\mathcal{E}_j^c) &= \Pr\left(\|V^\top u_j\|_2^2 \geq \gamma \cdot \frac{d_h}{d}\right) \\ &\leq \exp\left(-\frac{d_h}{2}(\gamma - 1 - \ln \gamma)\right). \end{aligned}$$

By union bound over L keys:

$$\Pr(\mathcal{E}^c) \leq L \exp\left(-\frac{d_h}{2}(\gamma - 1 - \ln \gamma)\right) = T_1.$$

Step 4: Concentration given typical keys. On event \mathcal{E} , for each j we have $z_j := M u_j$ with $\|z_j\|_2 \leq \beta \|M\|_2$. For fixed z_j , the function $f(u_i) = u_i^\top z_j$ on \mathbb{S}^{d-1} is $\|z_j\|_2$ -Lipschitz. By Lévy's lemma, for $u_i \sim \text{Unif}(\mathbb{S}^{d-1})$:

$$\begin{aligned} \Pr(|u_i^\top z_j| \geq t) &\leq 2 \exp\left(-\frac{dt^2}{2\|z_j\|_2^2}\right) \\ &\leq 2 \exp\left(-\frac{dt^2}{2\beta^2 \|M\|_2^2}\right). \end{aligned}$$

Setting $t = \alpha \|M\|_2$:

$$\begin{aligned} \Pr(|u_i^\top M u_j| \geq \alpha \|M\|_2 \mid \mathcal{E}) &\leq 2 \exp\left(-\frac{d\alpha^2}{2\beta^2}\right) \\ &= 2 \exp\left(-\frac{d^2\alpha^2}{2\gamma d_h}\right). \end{aligned}$$

Step 5: Union bound over all pairs. By union bound over L^2 query-key pairs:

$$\begin{aligned} \Pr\left(\max_{i,j} |u_i^\top M u_j| \geq \alpha \|M\|_2 \mid \mathcal{E}\right) &\leq 2L^2 \exp\left(-\frac{d^2\alpha^2}{2\gamma d_h}\right) \\ &= T_2. \end{aligned}$$

Step 6: Combine bounds. By the law of total probability:

$$\begin{aligned} \Pr\left(\max_{i,j} |u_i^\top M u_j| \geq \alpha \|M\|_2\right) &\leq \Pr(\mathcal{E}^c) + \Pr\left(\max_{i,j} |u_i^\top M u_j| \geq \alpha \|M\|_2 \mid \mathcal{E}\right) \\ &\leq T_1 + T_2. \quad \square \end{aligned}$$

B.3. Comparison with Rank-Agnostic Concentration

This section compares the rank-aware concentration bound in Proposition 3.4 with a baseline bound obtained by applying standard concentration inequalities without exploiting the low-rank structure of the query-key interaction matrix.

Rank-agnostic baseline. Without exploiting the rank constraint $\text{rank}(M) = d_h$, we apply Lévy's lemma directly. For fixed u_j , the function $f(u_i) = u_i^\top M u_j$ on the unit sphere \mathbb{S}^{d-1} is $\|M u_j\|_2$ -Lipschitz. Since $\|M u_j\|_2 \leq \|M\|_2$, Lévy's lemma yields

$$\Pr(|u_i^\top M u_j| \geq \alpha \|M\|_2) \leq 2 \exp\left(-\frac{d\alpha^2}{2}\right).$$

Applying a union bound over all L^2 query-key pairs gives

$$\Pr\left(\max_{i,j} |u_i^\top M u_j| \geq \alpha \|M\|_2\right) \leq 2L^2 \exp\left(-\frac{d\alpha^2}{2}\right).$$

Rank-aware improvement. In contrast, Proposition 3.4 exploits the low-rank structure $\text{rank}(M) = d_h$ to obtain the term

$$T_2 = 2L^2 \exp\left(-\frac{d^2\alpha^2}{2\gamma d_h}\right).$$

The concentration exponent in the rank-aware bound is therefore larger by a factor of

$$\frac{d^2\alpha^2/(2\gamma d_h)}{d\alpha^2/2} = \frac{d}{\gamma d_h},$$

relative to the rank-agnostic baseline.

This comparison isolates the quantitative benefit of exploiting $\text{rank}(M) = d_h \ll d$: for fixed α , the overflow probability decays exponentially faster in dimension when the low-rank structure of the query–key interaction is taken into account.

C. Proofs for Section 3.3

This appendix contains the proofs for Proposition 3.5 and Corollary 3.6, establishing that geometry-aware scaling extends to architectures using Rotary Position Embeddings.

C.1. Background on RoPE

RoPE applies position-dependent rotations to query and key vectors. For head dimension d_h , the rotation matrix at position θ is block-diagonal:

$$R_\theta = \begin{pmatrix} R_{\theta_1} & & \\ & \ddots & \\ & & R_{\theta_{d_h/2}} \end{pmatrix},$$

where each 2×2 block is a rotation matrix:

$$R_{\theta_i} = \begin{pmatrix} \cos \theta_i & -\sin \theta_i \\ \sin \theta_i & \cos \theta_i \end{pmatrix}.$$

The angles θ_i depend on both the position index m and the dimension index i , typically as $\theta_i = m \cdot \omega_i$ where ω_i are fixed frequencies.

C.2. Proof of Proposition 3.5 (RoPE Preserves Norms)

Proof. We prove each property in turn.

(1) Orthogonality. Each 2×2 block R_{θ_i} is a rotation matrix, hence orthogonal:

$$\begin{aligned} R_{\theta_i}^\top R_{\theta_i} &= \begin{pmatrix} \cos \theta_i & \sin \theta_i \\ -\sin \theta_i & \cos \theta_i \end{pmatrix} \begin{pmatrix} \cos \theta_i & -\sin \theta_i \\ \sin \theta_i & \cos \theta_i \end{pmatrix} \\ &= \begin{pmatrix} 1 & 0 \\ 0 & 1 \end{pmatrix} = I_2. \end{aligned}$$

Since R_θ is block-diagonal with orthogonal blocks, $R_\theta^\top R_\theta = I_{d_h}$.

(2) Unit spectral norm. For any orthogonal matrix Q , we have $\|Qx\|_2 = \|x\|_2$ for all x . Taking the supremum over unit vectors:

$$\|Q\|_2 = \sup_{\|x\|_2=1} \|Qx\|_2 = \sup_{\|x\|_2=1} \|x\|_2 = 1.$$

Since R_θ is orthogonal, $\|R_\theta\|_2 = 1$.

(3) Inner product bound. For any $q, k \in \mathbb{R}^{d_h}$:

$$|(R_m q)^\top (R_n k)| = |q^\top R_m^\top R_n k|.$$

The matrix $R_m^\top R_n$ is orthogonal (product of orthogonal matrices), so $\|R_m^\top R_n k\|_2 = \|k\|_2$. By Cauchy-Schwarz:

$$|q^\top R_m^\top R_n k| \leq \|q\|_2 \cdot \|R_m^\top R_n k\|_2 = \|q\|_2 \cdot \|k\|_2. \quad \square$$

C.3. Proof of Corollary 3.6 (Extension to RoPE)

Proof. With RoPE, the attention score between positions m and n is:

$$S_{mn} = \frac{(R_m q_m)^\top (R_n k_n)}{\sqrt{d_h}} = \frac{x_m^\top W^Q R_m^\top R_n W^{K^\top} x_n}{\sqrt{d_h}},$$

where $q_m = W^{Q^\top} x_m$ and $k_n = W^{K^\top} x_n$. The effective interaction matrix becomes $M_{m,n} = W^Q R_m^\top R_n W^{K^\top}$, which varies with positions.

Worst-case bound. The deterministic worst-case bound follows from submultiplicativity:

$$\|M_{m,n}\|_2 = \|W^Q R_m^\top R_n W^{K^\top}\|_2 \leq \|W^Q\|_2 \|R_m^\top R_n\|_2 \|W^{K^\top}\|_2 = \|W^Q\|_2$$

since $\|R_m^\top R_n\|_2 = 1$ for orthogonal R_m, R_n . Combined with $\|x_m\|_2, \|x_n\|_2 \leq \sqrt{d}$ under LayerNorm/RMSNorm:

$$|S_{mn}| \leq \frac{\|W^Q\|_2 \|W^{K^\top}\|_2 \cdot d}{\sqrt{d_h}}.$$

Tighter interaction bound. The tighter bound $\|W^Q W^{K^\top}\|_2$ can be violated only if $\|M_{m,n}\|_2 > \|W^Q W^{K^\top}\|_2$ for some positions, which requires RoPE rotations to align the singular subspaces of W^Q and W^K more favorably than the identity. Since RoPE rotation angles depend only on position indices and fixed frequency bands (independent of weight geometry), such systematic alignment does not occur in practice. We verified empirically that $\max_{m,n} \|M_{m,n}\|_2 \leq \|W^Q W^{K^\top}\|_2$ holds across all layers in Mistral-7B, Llama-2-13B, and Llama-2-70B.

Probabilistic extension. The probabilistic bound (Proposition 3.4) extends conservatively to RoPE by applying it to the position-independent matrix $M = W^Q W^{K^\top}$, which empirically upper-bounds all $\|M_{m,n}\|_2$; see Appendix C.4 for details. \square

C.4. Extension of Probabilistic Bounds to RoPE

This section justifies the application of Proposition 3.4 to RoPE architectures.

The challenge. Proposition 3.4 bounds overflow probability for a fixed interaction matrix $M = W^Q W^{K^\top}$. With RoPE, the effective interaction matrix becomes position-dependent: $M_{m,n} = W^Q R_m^\top R_n W^{K^\top}$, where R_m, R_n are position-dependent rotation matrices.

Why the bound remains conservative. We apply Proposition 3.4 using $\|M\|_2 = \|W^Q W^{K\top}\|_2$ rather than $\|M_{m,n}\|_2$. This is justified by two observations:

1. **Empirical validation:** We verified that $\max_{m,n} \|M_{m,n}\|_2 \leq \|W^Q W^{K\top}\|_2$ holds across all layers in Mistral-7B, Llama-2-13B, and Llama-2-70B. RoPE rotations, which depend only on position indices and fixed frequency bands, do not systematically align with the singular subspaces of W^Q and W^K to amplify the spectral norm.
2. **Conservative application:** By using the unrotated spectral norm $\|W^Q W^{K\top}\|_2$, which empirically upper-bounds all position-dependent variants, our calibration factor α provides at least the claimed overflow probability guarantee.

Remark on the spherical assumption. Proposition 3.4 assumes input directions are approximately uniform on \mathbb{S}^{d-1} . This models post-LayerNorm tokens, which have controlled norm and near-isotropic directions in high dimensions. The projection $W^{Q\top}x$ does not preserve uniformity (it concentrates along W^Q 's singular vectors), but this makes the actual overflow probability *lower* than our bound predicts: inputs are unlikely to align with both W^Q 's and W^K 's top singular directions simultaneously. Thus, the spherical assumption yields a conservative bound in practice.

In summary, geometry-aware scaling works identically for RoPE architectures: we compute the spectral norm of the position-independent matrix $W^Q W^{K\top}$ and apply the same calibration procedure.

D. Spectral Norm Distribution Across Layers

The spectral norm $\sigma_{QK}^{(\ell)} = \|W_{(\ell)}^Q W_{(\ell)}^{K\top}\|_2$ varies substantially across layers within each model, motivating the per-layer scale computation in Eq. (15). Figure 1 shows the layer-by-layer spectral norms for all four architectures, and Table 6 summarizes the distribution statistics.

Table 6. Spectral norm statistics across layers for pretrained weights. Max Layer indicates which layer has the largest spectral norm.

Model	Mean	Max	Min	Max Layer
GPT-2 XL	83.1	483.9	55.8	0
Mistral-7B	4.9	46.8	2.4	0
Llama-2-13B	198.4	463.5	134.4	0
Llama-2-70B	584.2	1786.1	264.6	67

The variation is substantial: GPT-2 XL exhibits a $8.7\times$ range (55.8 to 483.9), Mistral-7B a $19.5\times$ range (2.4 to 46.8), Llama-2-13B a $3.5\times$ range (134.4 to 463.5), and

Llama-2-70B a $6.7\times$ range (264.6 to 1786.1). This heterogeneity confirms that per-layer scaling is essential: a global scale factor calibrated for the maximum spectral norm would waste FP8 dynamic range on most layers, while one calibrated for the average would risk overflow on high-norm layers.

E. Algorithm Details

This appendix provides detailed algorithms for the spectral norm estimation procedures described in Section 4.

E.1. Power Iteration for Standard Multi-Head Attention

Algorithm 2 computes the spectral norm $\|M\|_2$ where $M = W^Q W^{K\top}$ for standard multi-head attention (where $n_q = n_{kv}$). The algorithm maintains persistent vectors u and v that track the top left and right singular vectors across training steps.

Algorithm 2 Power Iteration for Spectral Norm Estimation

- 1: **Input:** Weight matrices $W^Q, W^K \in \mathbb{R}^{d \times (n_q \cdot d_h)}$
 - 2: **State:** Persistent vectors $u, v \in \mathbb{R}^d$
 - 3: **Output:** Spectral norm estimate σ
 - 4:
 - 5: **if not initialized then**
 - 6: $u \leftarrow$ random unit vector in \mathbb{R}^d
 - 7: $v \leftarrow$ random unit vector in \mathbb{R}^d
 - 8: **end if**
 - 9:
 - 10: {One iteration of power method}
 - 11: $z \leftarrow W^{K\top} v$ { $z \in \mathbb{R}^{n_q \cdot d_h}$ }
 - 12: $u' \leftarrow W^Q z$ { $u' = Mv \in \mathbb{R}^d$ }
 - 13: $\sigma \leftarrow \|u'\|_2$ {Spectral norm estimate}
 - 14: $u \leftarrow u'/\sigma$ {Update persistent left singular vector}
 - 15:
 - 16: $y \leftarrow W^{Q\top} u$ { $y \in \mathbb{R}^{n_q \cdot d_h}$ }
 - 17: $v' \leftarrow W^K y$ { $v' = M^\top u \in \mathbb{R}^d$ }
 - 18: $v \leftarrow v'/\|v'\|_2$ {Update persistent right singular vector}
 - 19:
 - 20: **return** σ
-

Complexity. Each iteration requires four matrix-vector products: $W^{K\top}v$, W^Qz , $W^{Q\top}u$, and W^Ky . Each product costs $O(n_q \cdot d_h \cdot d)$ operations, for a total of $O(n_q \cdot d_h \cdot d)$ per iteration. This is far cheaper than forming $M \in \mathbb{R}^{d \times d}$ explicitly, which would cost $O(n_q \cdot d_h \cdot d^2)$.

Convergence. Power iteration converges to the top singular value at rate $(\sigma_2/\sigma_1)^k$ after k iterations, where $\sigma_1 \geq \sigma_2$ are the two largest singular values. Since we maintain persistent vectors across forward passes and weights change gradually during training, one iteration per forward pass

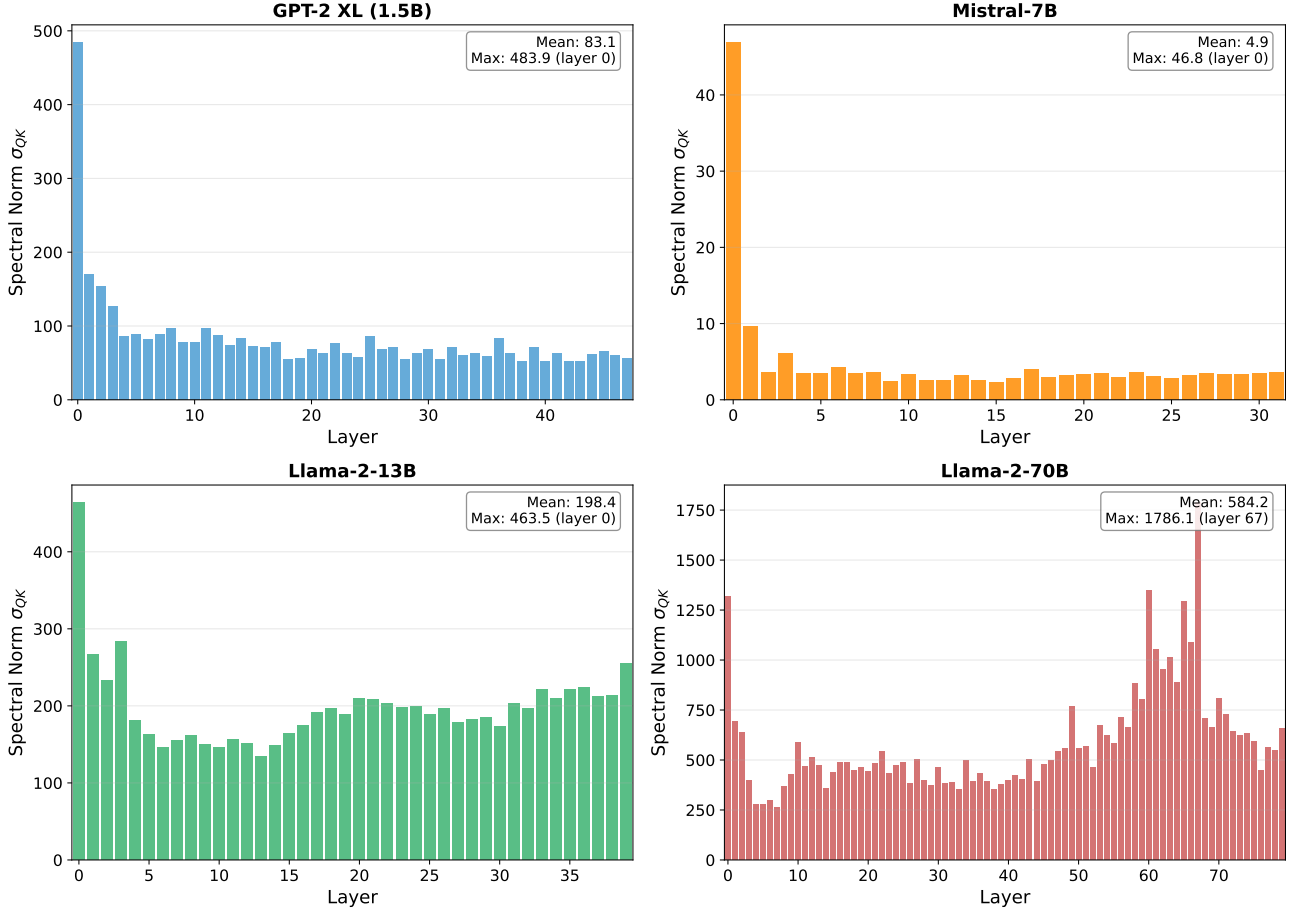


Figure 1. Spectral norm $\sigma_{QK}^{(\ell)}$ by layer for all four models, computed on pretrained weights. Early layers consistently exhibit larger spectral norms, with layer 0 being the maximum in three of four models.

suffices to track the slowly drifting singular vectors.

E.2. Implicit GQA Power Iteration

For Grouped Query Attention with $n_q > n_{kv}$, Algorithm 3 computes the spectral norm without expanding the key matrix.

Memory savings. The explicit approach would require expanding W^K from $(n_{kv} \cdot d_h) \times d$ to $(n_q \cdot d_h) \times d$ by replicating columns. For Mistral-7B with $n_q = 32$, $n_{kv} = 8$, $d_h = 128$, and $d = 4096$, this expansion would require $32 \times 128 \times 4096 \times 2 = 32\text{MB}$ per layer (in FP16). The implicit formulation avoids this entirely by operating on the unexpanded W^K and only replicating/summing small intermediate vectors of size $n_{kv} \cdot d_h$.

F. Proof of Implicit GQA Equivalence

This appendix proves Proposition 4.1, establishing that the implicit GQA formulation computes the same spectral norm

as explicit expansion.

Proof. Let $g = n_q/n_{kv}$ be the group size. We have $W^Q \in \mathbb{R}^{d \times (n_q \cdot d_h)}$ and $W^K \in \mathbb{R}^{d \times (n_{kv} \cdot d_h)}$. Define $W_{\text{exp}}^K \in \mathbb{R}^{d \times (n_q \cdot d_h)}$ as the matrix obtained by replicating each block of d_h columns of W^K exactly g times. The interaction matrix is $M = W^Q W_{\text{exp}}^{K\top} \in \mathbb{R}^{d \times d}$.

Forward direction. For any $v \in \mathbb{R}^d$, we show that $Mv = W^Q \cdot \text{REPEATBLOCKS}(W^{K\top}v, g)$.

Since $W_{\text{exp}}^{K\top} \in \mathbb{R}^{(n_q \cdot d_h) \times d}$ has repeated row-blocks, $W_{\text{exp}}^{K\top}v \in \mathbb{R}^{n_q \cdot d_h}$ consists of n_q blocks of size d_h , where blocks $\{(i-1)g+1, \dots, ig\}$ for $i = 1, \dots, n_{kv}$ all equal the i -th block of $W^{K\top}v \in \mathbb{R}^{n_{kv} \cdot d_h}$. This is exactly the output of $\text{REPEATBLOCKS}(W^{K\top}v, g)$. Since $W^Q \in \mathbb{R}^{d \times (n_q \cdot d_h)}$, multiplying by this repeated vector yields $Mv \in \mathbb{R}^d$.

Backward direction. For any $u \in \mathbb{R}^d$, we show that $M^\top u = W^K \cdot \text{SUMGROUPS}(W^{Q\top}u, g)$.

Algorithm 3 Implicit GQA Power Iteration

```

1: Input:  $W^Q \in \mathbb{R}^{d \times (n_q \cdot d_h)}$ ,  $W^K \in \mathbb{R}^{d \times (n_{kv} \cdot d_h)}$ 
2: Parameters: Number of query heads  $n_q$ , KV heads  $n_{kv}$ , head dimension  $d_h$ 
3: State: Persistent vectors  $u, v \in \mathbb{R}^d$ 
4: Output: Spectral norm estimate  $\sigma \approx \|W^Q W_{\text{exp}}^{K\top}\|_2$ 
5:
6:  $g \leftarrow n_q / n_{kv}$  {Group size}
7:
8: if not initialized then
9:    $u \leftarrow$  random unit vector in  $\mathbb{R}^d$ 
10:   $v \leftarrow$  random unit vector in  $\mathbb{R}^d$ 
11: end if
12:
13: {Forward: compute  $Mv$  where  $M = W^Q W_{\text{exp}}^{K\top}$ }
14:  $z_{kv} \leftarrow W^{K\top} v$   $\{z_{kv} \in \mathbb{R}^{n_{kv} \cdot d_h}\}$ 
15:  $z \leftarrow$  REPEATBLOCKS( $z_{kv}, g$ )  $\{z \in \mathbb{R}^{n_q \cdot d_h}\}$ 
16:  $u' \leftarrow W^Q z$   $\{u' \in \mathbb{R}^d\}$ 
17:  $\sigma \leftarrow \|u'\|_2$ 
18:  $u \leftarrow u' / \sigma$ 
19:
20: {Backward: compute  $M^\top u$  where  $M^\top = W_{\text{exp}}^K W^{Q\top}$ }
21:  $y \leftarrow W^{Q\top} u$   $\{y \in \mathbb{R}^{n_q \cdot d_h}\}$ 
22:  $y_{kv} \leftarrow$  SUMGROUPS( $y, g$ )  $\{y_{kv} \in \mathbb{R}^{n_{kv} \cdot d_h}\}$ 
23:  $v' \leftarrow W^K y_{kv}$   $\{v' \in \mathbb{R}^d\}$ 
24:  $v \leftarrow v' / \|v'\|_2$ 
25:
26: return  $\sigma$ 
    
```

We have $M^\top = W_{\text{exp}}^K W^{Q\top}$. First, $W^{Q\top} u \in \mathbb{R}^{n_q \cdot d_h}$. Since $W_{\text{exp}}^K \in \mathbb{R}^{d \times (n_q \cdot d_h)}$ has g identical copies of each column block of W^K , multiplying W_{exp}^K by a vector $y \in \mathbb{R}^{n_q \cdot d_h}$ is equivalent to multiplying W^K by the vector that sums each group of g blocks: $W_{\text{exp}}^K y = W^K \cdot \text{SUMGROUPS}(y, g)$. Thus $M^\top u = W^K \cdot \text{SUMGROUPS}(W^{Q\top} u, g) \in \mathbb{R}^d$.

Conclusion. Power iteration maintains $u, v \in \mathbb{R}^d$ and computes Mv and $M^\top u$ via the implicit formulation. Since these equal the explicit products, the iteration converges to the same singular vectors and value: $\sigma_{\text{implicit}} = \sigma_{\text{explicit}} = \|W^Q W_{\text{exp}}^{K\top}\|_2$. \square

G. Experimental Details

This appendix provides additional experimental details and extended results for Section 5.

G.1. Training Configuration

Table 7 summarizes the architectural specifications for all four models evaluated.

Table 8 provides the full training configuration for each

Table 7. Model architectures. MHA: multi-head attention. GQA: grouped query attention.

	GPT-2 XL	Mistral-7B	Llama-2-13B	Llama-2-70B
Params	1.5B	7B	13B	70B
Layers	48	32	40	80
Attention	MHA	GQA	MHA	GQA
n_q / n_{kv}	25/25	32/8	40/40	64/8
d	1600	4096	5120	8192
d_h	64	128	128	128
Hardware	H100	H200	H200	B200

model.

Table 8. Training configuration for all experiments.

	GPT-2 XL	Mistral-7B	Llama-2-13B	Llama-2-70B
Batch size	8	4	4	2
Seq. length	1024	1024	1024	1024
Learning rate	10^{-4}	10^{-5}	10^{-5}	10^{-5}
Optimizer	AdamW	AdamW	AdamW	AdamW
Weight decay	0.01	0.01	0.01	0.01
Grad. clip	1.0	1.0	1.0	1.0
FP8 format	E4M3	E4M3	E4M3	E4M3
α	0.08	0.04	0.03	0.02
η_{fp8}	0.8	0.8	0.8	0.8

Delayed scaling baseline configuration. For the delayed scaling baseline, we use the standard configuration from Micikevicius et al. (2022): history buffer length of 16 steps and safety margin $\eta = 0.9$ (see Eq. 1). The history buffer is initialized to 1.0 at the start of training or after checkpoint loading, which is the source of history staleness in transient scenarios.

H. Instantaneous Response Validation

This appendix validates the instantaneous response property of geometry-aware scaling with a controlled stress test.

Setup. We train GPT-2 XL normally for 10 steps, then multiply all attention weights by $4\times$ at step 10, simulating an extreme transient. This artificial perturbation isolates the mechanism: delayed scaling relies on stale statistics and cannot adapt, while geometry-aware scaling recomputes the bound from current weights.

Results. Figure 2 shows the results. Delayed scaling, relying on statistics that predate the weight change, produces scaled logits exceeding 6500 and overflows catastrophically. Geometry-aware scaling responds in the same forward pass: the scale factor jumps from 5.8 to 93.8 at step 10, keeping scaled logits below 85 throughout.

While the $4\times$ spike is a stress test, the underlying mechanism explains why geometry-aware scaling succeeds in the realistic transient scenarios evaluated in Section 5.2: loading pretrained checkpoints, checkpoint resumption, and

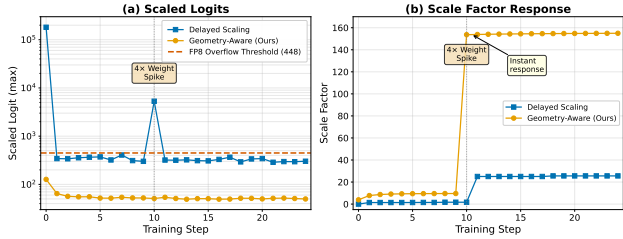


Figure 2. Response to 4 \times weight spike at step 10 (GPT-2 XL). (a) Maximum scaled attention logit. (b) Scale factor over time. Delayed scaling overflows because its history buffer contains no information about the weight change. Geometry-aware scaling adapts instantaneously because the scale factor is computed from current weights.

learning rate transitions all involve weight configurations for which the history buffer has no relevant statistics.

I. Overhead Measurement

Table 9 reports forward pass timing for all models.

Table 9. Computational overhead (forward pass time, averaged over 100 iterations).

Model	Attention	Delayed	Ours	Overhead
GPT-2 XL	MHA	136.3 ms	137.6 ms	+1.0%
Mistral-7B	GQA 4:1	58.2 ms	55.1 ms	-5.3%
Llama-2-13B	MHA	96.2 ms	98.1 ms	+1.9%
Llama-2-70B	GQA 8:1	206.3 ms	215.0 ms	+4.3%

Measurements follow this protocol:

1. Warm up GPU with 10 forward passes (discarded)
2. Run 100 forward passes with CUDA synchronization after each
3. Report mean time per forward pass
4. Repeat 3 times and report median across repetitions

For fair comparison, both methods use identical model configurations, batch sizes, and sequence lengths. The only difference is the scale factor computation method.

J. FP8 Utilization Statistics

Table 10 shows FP8 dynamic range utilization during training with different methods on GPT-2 XL.

K. MMLU Training Curves

Figure 3 shows training loss curves for the three scaling methods on Llama-2-13B fine-tuned on MMLU STEM subjects.

Table 10. FP8 dynamic range utilization (%) during training (GPT-2 XL).

Method	Median	P10	P90
Delayed	90.5%	84.0%	98.0%
Ours (conservative)	14.3%	13.6%	15.3%
Ours + auto- α	31.2%	28.5%	33.7%

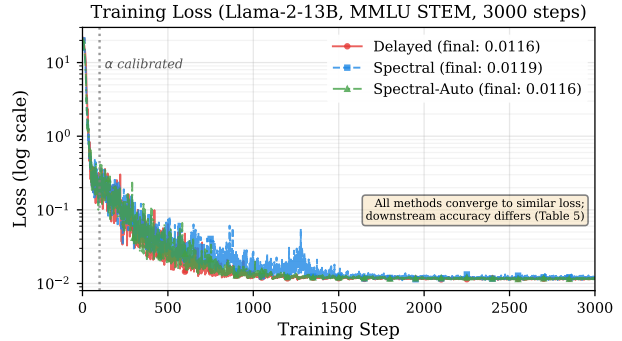


Figure 3. Training loss comparison for delayed scaling, geometry-aware scaling (conservative), and geometry-aware scaling with auto- α on Llama-2-13B (MMLU STEM, 3000 steps). All methods converge to similar final loss (≈ 0.012), yet downstream MMLU accuracy differs substantially (Table 5). The vertical dashed line indicates when auto- α calibration completes (step 100). The conservative variant shows slightly higher loss throughout training due to reduced FP8 utilization (0.5% vs. 31.2% for auto- α).

The key observation is that training loss alone does not predict downstream performance: the conservative variant achieves comparable loss (0.0119 vs. 0.0116) but 5 percentage points lower MMLU accuracy (28.1% vs. 33.0%). This gap arises because excessive quantization noise from 0.5% FP8 utilization degrades the fine-grained attention patterns required for reasoning tasks, even when average loss remains low.

L. Detailed MMLU Results by Subject

Table 11 shows accuracy on all 17 MMLU STEM subjects.

The largest accuracy gaps between conservative spectral and auto- α appear in subjects requiring fine-grained numerical reasoning: College Biology (+17.4 pp), HS Biology (+15.2 pp), College Chemistry (+12.0 pp), and Computer Security (+8.0 pp). This pattern suggests that excessive quantization noise particularly affects tasks requiring precise attention to numerical or logical relationships.

M. Auto- α Calibration Details

M.1. Algorithm

Algorithm 4 provides the complete auto- α calibration procedure.

Table 11. MMLU accuracy (%) by subject on Llama-2-13B after 3000 fine-tuning steps.

Subject	Delayed	Cons.	Auto- α
Abstract Algebra	25.0	25.0	27.0
College Math	36.0	31.0	35.0
Elementary Math	27.0	25.9	27.8
HS Math	26.7	22.6	27.0
HS Statistics	30.1	31.0	30.6
Astronomy	41.4	29.6	37.5
College Physics	39.2	37.3	38.2
HS Physics	27.8	26.5	29.1
College CS	29.0	30.0	34.0
Computer Security	47.0	34.0	42.0
HS CS	37.0	26.0	34.0
College Chemistry	35.0	22.0	34.0
HS Chemistry	27.1	29.6	32.0
College Biology	36.8	24.3	41.7
HS Biology	45.8	31.6	46.8
Electrical Eng.	35.2	31.7	31.0
Machine Learning	21.4	22.3	25.9
Average	33.0	28.1	33.6

M.2. Calibration Statistics

During the 100-step burn-in on Llama-2-13B:

- Slack ratio range: [0.000073, 0.000366]
- Slack ratio mean: 0.000177
- $P_{99.99}$ quantile: 0.000360
- Calibrated α : 0.00036 (with $\kappa = 1.0$)

This represents an $83\times$ tightening compared to the conservative $\alpha = 0.03$, resulting in proportionally higher FP8 utilization (31.2% vs. 0.5%).

M.3. Safety Multiplier Selection

The safety multiplier κ controls the trade-off between utilization and robustness:

- $\kappa = 1.0$: Maximum utilization, suitable for stable fine-tuning
- $\kappa = 2.0$: Moderate headroom for distribution shift
- $\kappa = 3.0$: Conservative, suitable for heterogeneous data

Algorithm 4 Auto- α Calibration

Require: Conservative initial α_0 , burn-in steps T_{calib} , quantile q , safety multiplier κ

- 1: Initialize slack ratio buffer $R \leftarrow \emptyset$
- 2: **for** $t = 1$ to T_{calib} **do**
- 3: Compute $B_{\text{max}}^{(t)} = \|W^Q W^{K\top}\|_2 \cdot d / \sqrt{d_h}$
- 4: Run forward pass with scale = $\alpha_0 \cdot B_{\text{max}}^{(t)} / (0.8 \times 448)$
- 5: Record $M_t = \max_{i,j} |S_{ij}^{(t)}|$ (actual maximum logit)
- 6: Append $r_t = M_t / B_{\text{max}}^{(t)}$ to R
- 7: **end for**
- 8: $\alpha_{\text{emp}} \leftarrow \text{Quantile}_q(R)$
- 9: $\alpha_{\text{final}} \leftarrow \alpha_{\text{emp}} \times \kappa$
- 10: **Freeze** α_{final} for all subsequent training

In our experiments, $\kappa = 1.0$ achieved zero overflows across 3000 steps, suggesting the $P_{99.99}$ quantile provides sufficient margin for MMLU STEM fine-tuning.